Materialia 7 (2019) 100372

Contents lists available at ScienceDirect

Materialia

journal homepage: www.elsevier.com/locate/mtla

Full Length Article

Septenary Zr–Hf–Ti–Al–Co–Ni–Cu high-entropy bulk metallic glasses with centimeter-scale glass-forming ability

Takeshi Wada [a,*], Jing Jiang [a], Kunio Yubuta [a], Hidemi Kato [a], Akira Takeuchi [b]

[a] Institute for Materials Research, Tohoku University, 2-1-1 Katahira, Aoba-ku, Sendai 980-8577, Japan
[b] Graduate School of Engineering, Tohoku University, 6-6-01-2 Aoba, Aramaki, Aoba-ku, Sendai 980-8579, Japan

ARTICLE INFO

Keywords:
Bulk metallic glass
Eutectic solidification
High-entropy alloy

ABSTRACT

A new $Zr_{35}Hf_{17.5}Ti_{5.5}Al_{12.5}Co_{7.5}Ni_{12}Cu_{10}$ high-entropy bulk metallic glass with glass-forming ability up to centimeter scale (diameter of 18 mm) and configuration entropy of 1.77*R* was discovered. This high-entropy bulk metallic glass differs from previous ones because it was designed to possess a non-equiatomic eutectic composition and was free from Be. The high-entropy alloy exhibited excellent glass-forming ability despite its lower reduced glass transition temperature than those of prototypical glasses. Molecular dynamics simulations suggested that the excellent glass-forming ability was caused by the similar magnitude of the decrease in Hamiltonian from amorphous to crystalline phases to that of a reference ternary bulk metallic glass, as well as the sluggish crystallization of the high-entropy bulk metallic glass.

Advanced materials including high-entropy alloys (HEAs) and bulk metallic glasses (BMGs) are attracting attention in materials science [1–5]. Generally, HEAs contain more than five components with exact or near equiatomic composition and form single solid solutions with simple face-centered cubic, body-centered cubic, or hexagonal close-packed structures. The four core effects [2] of HEAs, which are high entropy, sluggish diffusion, severe lattice distortion, and cocktail effects, result in attractive properties that differ from those of conventional alloys [3,4]. BMGs are multicomponent alloys with a disordered atomic arrangement that are generally prepared by rapid solidification. The absence of long-range periodicity in the structure of BMGs induces various superior properties compared with those of crystalline counterparts [6–8]. Combining the advantage of both HEAs and BMGs, high-entropy bulk metallic glasses (HE-BMGs) were recently developed. HE-BMGs with a dimension larger than 1 mm reported to date include $Ti_{20}Zr_{20}Hf_{20}Cu_{20}Ni_{20}$ [9], $Pd_{20}Pt_{20}Cu_{20}Ni_{20}P_{20}$ [10], $Sr_{20}Ca_{20}Yb_{20}(Mg,Li)_{20}(Zn,Cu)_{20}$ [11], $Ti_{20}Zr_{20}Cu_{20}Ni_{20}Be_{20}$ [12], $Ti_{20}Zr_{20}Hf_{20}Be_{20}(Cu,Ni)_{20}$ [13,14], $Ti_{16.7}Zr_{16.7}Hf_{16.7}Be_{16.7}Cu_{16.7}Ni_{16.7}$ [15], $Gd_{20}Tb_{20}Dy_{20}Al_{20}(Co,Fe,Ni)_{20}$ [16], and $Fe_{25}Co_{25}Ni_{25}(P,C,B,Si)_{25}$ [17,18]. Although the glass-forming ability (GFA) of some HE-BMGs reaches the centimeter scale [10,13–15,19], they tend to have lower GFAs than those of prototypical BMGs. The correlation between GFA and configuration entropy (S_{config}) is under debate and two opposite effects of entropy on GFA have been proposed. One is that the GFA increases with the number of components because of the lower chance that the alloy can select a viable crystal structure, which known as the confusion principle [20]. The second is that the GFA decreases because of the lower viscosity of a liquid with higher S_{config}, which known as the Adam–Gibbs theory [21]. The extent to which these two entropic factors affect the GFA of alloys has not been clarified.

Because previously reported HE-BMGs were developed based on the concept of high entropy, equiatomic composition was regarded as the most important factor to maximize S_{config}. However, as shown in a number of previous studies on BMGs, a high GFA of a system is closely related to the eutectic point, which is generally expressed by non-equiatomic composition; for example, $Zr_{50}Al_{10}Cu_{40}$ [22] and $Zr_{56}Al_{16}Co_{28}$ [23]. The high GFA of systems with non-equiatomic compositions is also related to atomic fractions of solutes enabling dense packing of atomic clusters, which is determined by the ratio of solute to solvent radius [24]. These factors indicate that maximum GFA is not necessarily compatible with maximum entropy, which led us to consider that it may be possible to obtain HE-BMGs with excellent GFA in non-equiatomic composition. According to Yeh [3], an HEA is defined by two criteria; one is based on composition (number of components $n \geq 5$ and concentration of the *i*th component x_i, $5 < x_i < 35$ at.%), and the other is based on S_{config} ($S_{config} = -R\sum_{i=1}^{n} x_i \ln(x_i) > 1.5R$, where R is the gas constant). Following these two criteria, we searched for new HE-BMGs with excellent GFA. For the composition exploration, a prototypical metallic glass composition was modified by substituting its constituents with other elements with similar chemical properties and atomic radius. Using this strategy, several types of new HE-BMGs were successfully prepared [10,19,25].

* Corresponding author.
E-mail address: wada-t@imr.tohoku.ac.jp (T. Wada).

https://doi.org/10.1016/j.mtla.2019.100372
Received 30 May 2019; Accepted 3 June 2019
Available online 7 June 2019

It should be noted that such substitution strongly affects entropy but only weakly influences enthalpy because the mixing enthalpy between the constituent and substituent elements is nearly zero, allowing us to examine the effect of entropy on GFA.

Quaternary to septenary alloys of (Zr, Hf, Ti)-Al-(Co, Ni, Cu) were prepared by arc melting under high-purity Ar gas atmosphere using pure metals (>99.9 mass%). The structure of the samples was examined by X-ray diffraction (XRD) using Cu Kα radiation (Rigaku Ultima IV). Microstructure and composition were analyzed by scanning electron microscopy-energy-dispersive X-ray spectroscopy (SEM-EDX) on a Zeiss Ultra 55 microscope with a Bruker X-flash 4010 detector. High-resolution transmission electron microscopy (HR-TEM) images were collected on a TOPCON EM-002B microscope. Glass transition, crystallization, liquidus, and solidus temperatures were analyzed by differential scanning calorimetry (DSC; TA Instruments SDT-600 and Q100). GFAs of the alloys were evaluated by measuring the maximum glass formation diameter obtained by arc-melting tilt casting using a Cu mold. Molecular dynamics (MD) simulations were performed with SCIGRESS ME Version 2.3 [26] for amorphous, chemically disordered body-centered cubic (bcc), Zr_6Al_2Co and chemically ordered CoZr (B2) phases [27]. An *NTp* ensemble that maintained the number of atoms (N), temperature (T), and pressure (p; 101.325 kPa) as constants was used under periodic boundary conditions with a time step of 0.1 fs. The generalized embedded atom method (GEAM) MD potential provided in the software [26], which is based on the embedded atom method [28], was used in the simulation because of its wide applicability to pure elements and alloys. However, the GEAM potential does not possess the parameters for Hf, so they were estimated from those of Zr using the chemical and physical similarities between Hf and Zr, as performed elsewhere [29]. Reported crystallographic data for Zr_6Al_2Co [30] and CoZr [27] were used to obtain lattice constants and coordinates of sites in the unit cell. As the initial atomic configurations for simulations, 2000 atoms in $10\times10\times10$ supercells with a cubic structure were adopted for the amorphous, bcc, and CoZr phases using the lattice constants of the CoZr phase [27], whereas 2250 atoms in a $5\times5\times10$ supercell with a hexagonal structure were obtained from the data for the Zr_6Al_2Co phase [30]. The constituent atoms of the initial states of the amorphous and bcc phases were randomly distributed at sites in the supercell. The constituent atoms of the initial states were randomly distributed within each site of α- and β-sublattices for the CoZr phase and were at Zr, Al, and Co sites for the Zr_6Al_2Co phase.

Specifically, the site occupation of the constituent elements in the initial states were treated as follows. For the multicomponent Zr_6Al_2Co phase, Ti, Zr, and Hf were regarded as Zr-family elements and Co, Ni, and Cu were considered Co-family elements. For the multicomponent CoZr phase, Al occupied the Co sites. In accordance with the above site occupation, the differences in composition between the experimentally obtained CoZr phase from the stoichiometric one were compensated for by converting the excess atoms above the stoichiometry to the other sublattice. In a similar manner, the excess atoms above the stoichiometry for each site of Zr, Al, and Co were moved to other sites for the Zr_6Al_2Co phase.

The bcc, CoZr, and Zr_6Al_2Co phases were structurally relaxed at 100 K for 0.1 ps before annealing at 973 K for 1 ps. In contrast, the amorphous phase was generated through a process of melting, quenching, and structural relaxation by thermal treatment at 4500 K for 0.2 ps, cooling at a rate of 10^{14} K/s from 4500 to 500 K, and holding at 500 K for 0.4 ps, respectively. The relaxed amorphous phase was then annealed at 973 K for 1 ps. During the simulations, the Hamiltonian ($\mathcal{H}$) was monitored to evaluate the phase stability (energy level) [31] of the phases in place of the Gibbs free energy in the thermodynamic analysis. In addition, the self-diffusion coefficient of X element (D_X) was calculated for the amorphous phases that were annealed at 973 K for 1 ps. D_X values were calculated using the software from the mean square displacements of X element ($L_{MSD,X}$) [29] and computation time (t) using the widely known formula $D_X = \lim_{t\to\infty}\{d(\langle L_{MSD,X}\rangle)/dt\}/6$.

Because the HE-BMGs being studied possessed $n > 5$, experiments for all compositions would be very time-consuming. For efficiency, we first investigated more than 30 different compositions with a relatively large interval (5 at.%) to cover a wide compositional range. As a quick evaluation of GFA, we carefully observed the undercooling behavior and surface morphology of the ingots after arc melting. It is empirically known that alloys with high GFA show large undercooling and smooth surfaces after solidification because of their fine microstructure and homogeneous volume shrinkage. Among the alloys investigated initially, several candidates for further study were selected and precise composition tuning was performed based on their thermal and microstructural analyses.

The effect of partial substitution of Zr by Hf and Ti in the $Zr_{55}Al_{20}Co_{25}$ alloy was investigated next. Because Hf and Ti form a solid solution with Zr at any ratio, high interchangeability without losing GFA was expected. Quaternary $Zr_{30}Ti_{25}Al_{20}Co_{25}$ and $Zr_{30}Hf_{25}Al_{20}Co_{25}$ alloys were prepared. The surface morphology of the obtained ingots is shown in Fig. 1a. Note that the ingots have nearly the same mass of 5 g, which means that they solidified at almost the same cooling rate. In the Ti-substituted alloy, well-grown crystals are visible and the surface is rough because of inhomogeneous volume shrinkage, whereas the Hf-substituted alloy has a very smooth mirror-like surface. Large undercooling after arc melting was observed for the Hf-substituted alloy, whereas the Ti-substituted alloy instantaneously crystallized from higher temperature just after the heating stopped. The GFAs of these alloys were analyzed by casting using a Cu mold. XRD patterns of the cast rods with a diameter of 5 mm are shown in Fig. 1b. The Ti-substituted alloy rod displayed intense peaks that were identified as the hexagonal ZrAlCo phase (ICSD: 606728, space group: P63/mmc, $a = 0.5212$ nm, and $c = 0.8453$ nm) and no evidence of glass formation was seen. In contrast, the Hf-substituted alloy rod mainly showed broad diffraction peaks consistent with glassy structure, indicating that Hf substitution can retain the GFA of $Zr_{55}Al_{20}Co_{25}$ alloy. The marked difference in the interchangeability of Ti (atomic radius $r_{Ti} = 0.147$ nm) and Hf ($r_{Hf} = 0.160$ nm) with Zr ($r_{Zr} = 0.162$ nm) probably originates from the difference between the atomic radii of Ti and Zr. The mismatch in atomic size between Ti and Zr made it difficult for Ti to dissolve in the Zr-based compounds in large amounts, so it was rejected and formed another compound with high melting temperature. Therefore, we selected $Zr_{30}Hf_{25}Al_{20}Co_{25}$ for further investigation.

In the next step, part of the Co in $Zr_{30}Hf_{25}Al_{20}Co_{25}$ was replaced by Ni and/or Cu to give alloys with the general formula $Zr_{30}Hf_{25}Al_{20}Co_{25-x-y}Ni_xCu_y$. It was found that Ni and Cu had high interchangeability with Co and glass formation occurred over a wide composition range of $0 < x+y < 25$. Among the compositions investigated, $Zr_{30}Hf_{25}Al_{20}Co_{10}Ni_{10}Cu_5$ was selected because of its large undercooling. Fig. 2a shows a cast rod of $Zr_{30}Hf_{25}Al_{20}Co_{10}Ni_{10}Cu_5$ with a diameter of 12 mm, which has a smooth surface. The HR-TEM image in Fig. 2b, which was taken from the center of the rod cross section, reveals the atomically disordered structure of the alloy. The $Zr_{30}Hf_{25}Al_{20}Co_{10}Ni_{10}Cu_5$ alloy achieved a centimeter-scale GFA of 12 mm, which was the best GFA obtained in the composition exploration with a 5 at.% interval.

The last step was precise composition tuning based on thermal and microstructure analyses. Fig. 2c presents DSC curves of the melting and solidification of the $Zr_{30}Hf_{25}Al_{20}Co_{10}Ni_{10}Cu_5$ alloy. Upon melting/solidification, the alloy showed more than two separated endo/exothermic peaks, suggesting the alloy has off-eutectic composition. The microstructure of the solidified alloy displayed in Fig. 2d showed the precipitation of faceted primary crystals with dark contrast (indicated by an arrow) embedded in the fine eutectic microstructure. SEM-EDX analysis revealed that this dark-contrast phase has a composition of $Zr_{19.5}Hf_{14.6}Al_{34.7}Co_{11.2}Ni_{16.9}Cu_{3.1}$, which is enriched in Al with respect to the nominal composition, indicating the remaining eutectic liquid should contain less Al than the nominal composition. By calculating the volume fraction of the primary phase from the

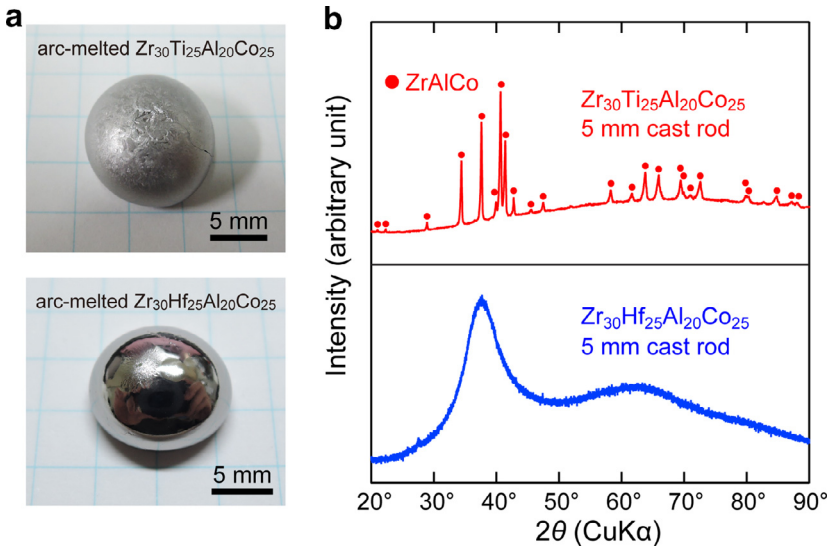

Fig. 1. (a) Surface morphology of $Zr_{30}Ti_{25}Al_{20}Co_{25}$ and $Zr_{30}Hf_{25}Al_{20}Co_{25}$ ingots (5 g) solidified after arc melting. (b) XRD patterns of $Zr_{30}Ti_{25}Al_{20}Co_{25}$ and $Zr_{30}Hf_{25}Al_{20}Co_{25}$ alloy rods with a diameter of 5 mm prepared by tilt casting.

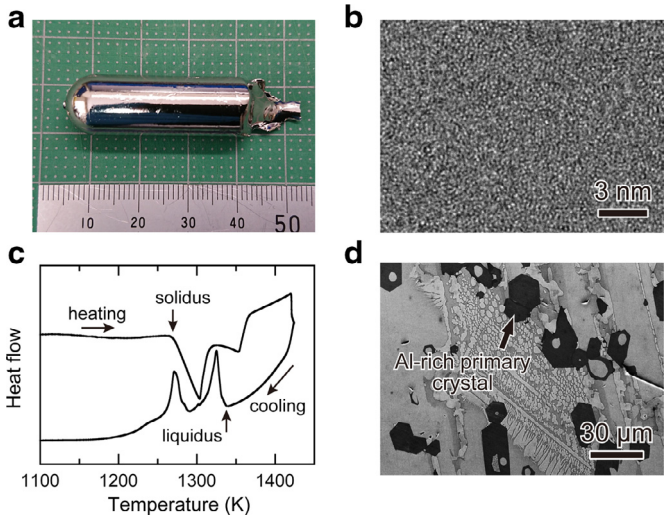

Fig. 2. (a) Photograph and (b) HR-TEM image of a $Zr_{30}Hf_{25}Al_{20}Co_{10}Ni_{10}Cu_5$ alloy cast rod with a diameter of 12 mm prepared by tilt casting. (c) DSC curve for melting/solidification and (d) microstructure of solidified $Zr_{30}Hf_{25}Al_{20}Co_{10}Ni_{10}Cu_5$ alloy.

SEM image, the composition of the remaining liquid was estimated and an ingot with this composition was then produced by arc melting. By repeating these thermal and microstructural analyses, the composition of the alloy was precisely tuned. Finally, the composition of $Zr_{35}Hf_{17.5}Ti_{5.5}Al_{12.5}Co_{7.5}Ni_{12}Cu_{10}$ was reached. The DSC curve of the alloy in Fig. 3a shows overlapping endothermic peaks over a wide range of about 100 K during heating, indicating several melting reactions occur. In the cooling process, the alloy solidified with almost single narrow exothermic peak. Fig. 3b presents a backscattered electron micrograph for the solidified alloy after DSC testing. The alloy has complex eutectic microstructure with at least three phases and is mainly composed of a binary eutectic of ZrCo (bright contrast) and Zr_6Al_2Co (intermediate contrast). A binary eutectic of ZrCo and Al-rich phases (dark contrast) and ternary eutectic (shown in the inset of Fig. 3(b)) were also observed with moderate volume fractions. This implies that the alloy was not located exactly at the eutectic point and thus multiple eutectic reactions occurred. However, the lack of obvious primary crystals in the microstructure and the sharp exothermic peak in the DSC cooling trace suggest that the composition is close to the eutectic point. The GFA of this $Zr_{35}Hf_{17.5}Ti_{5.5}Al_{12.5}Co_{7.5}Ni_{12}Cu_{10}$ alloy was investigated by tilt casting. As shown in the inset of Fig. 3c, the cast rod with a diameter of 18 mm possessed a very smooth and shiny surface. The XRD pattern in Fig. 3c measured from the center of the cross section at the middle of the rod contained broad diffraction peaks. The EDX mapping in Fig. 3d confirmed the uniform distribution of elements in the alloy; no compositional fluctuation was detected despite the seven components. All of these features indicated that the cast rod possessed a fully glassy structure. These results confirmed that the $Zr_{35}Hf_{17.5}Ti_{5.5}Al_{12.5}Co_{7.5}Ni_{12}Cu_{10}$ alloy had excellent GFA of up to 18 mm in conjunction with a high S_{config} of 1.77R. This work demonstrated that the strategy of searching for eutectic composition in a multicomponent alloy is effective to develop HE-BMGs with high GFA. To date, a series of Be-bearing alloys (~30 mm) [13–15] and $Zr_{40}Hf_{10}Ti_4Y_1Al_{10}Cu_{25}Ni_7Co_2Fe_1$ (14 mm) [19] have been reported as centimeter-scale HE-BMGs in the metalloid-free alloy systems. The Be-free HE-BMG with good GFA developed in this work represents another type of centimeter-scale HE-BMG.

Here we discuss the effect of entropy on GFA. Table 1 summarizes the maximum glass formation diameter (D_{max}), glass transition temperature (T_g), liquidus (T_l), reduced glass transition temperature (T_g/T_l), and configuration entropy normalized by the gas constant ($S_{config.}/R$) of the developed HE-BMGs, together with those of previously reported similar Zr-based HE-BMG and normal BMGs [19,23,32,33]. Although the Zr-based HE-BMG and BMGs are similar in terms of a general formula of $ETM_{50–60}Al_{10–20}LTM_{20–40}$, where ETM and LTM are early and late transition metals, respectively, their GFA varies drastically. In addition, there is no correlation between D_{max} and $S_{config.}$, indicating that $S_{config.}$ is not a direct measure of GFA in these systems. Among the various alloys in Table 1, it is interesting to compare the GFAs of $Zr_{35}Hf_{17.5}Ti_{5.5}Al_{12.5}Co_{7.5}Ni_{12}Cu_{10}$ (hereafter called Zr-HE-BMG) and $Zr_{56}Al_{16}Co_{28}$ (hereafter called Zr-BMG) because both of these alloys are located near the eutectic point and mainly crystallize into compounds with the same crystal structures but have a large difference between their S_{config} values. D_{max} for the Zr-HE-BMG was 18 mm, which is the same as that reported for Zr-BMG [23], even though Zr-HE-BMG (1.77R) has much higher S_{config} than the Zr-BMG (0.97R). Fig. 4a shows XRD patterns for Zr-BMG and Zr-HE-BMG ribbons annealed for 12 h at 973 K, which is about 200 K higher than the crystallization temperature of these alloys. In Zr-BMG, the main crystallized phases are cubic ZrCo (ICSD: 625704, space group: Pm-3 m, and $a = 0.3203$ nm) and hexagonal Zr_6Al_2Co (ICSD: 150575, space group: P-62 m, $a = 0.7902$ nm, and $c = 0.3360$ nm). In Zr-HE-BMG, the main crystallized phases are the same as those of Zr-BMG but their

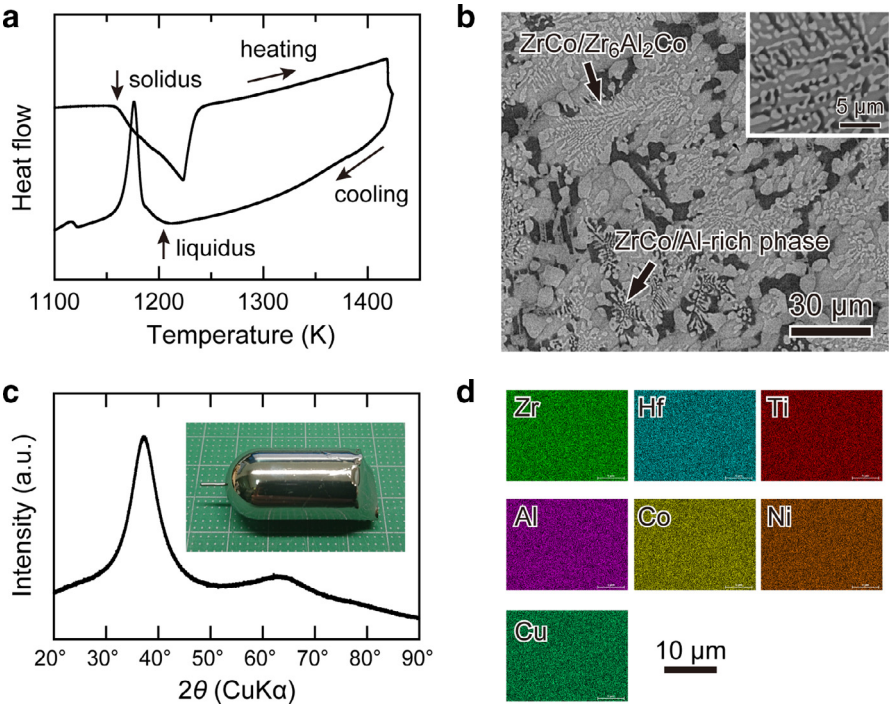

Fig. 3. (a) DSC curve showing melting/solidification at 10 K/min and (b) corresponding solidified microstructure of the $Zr_{35}Hf_{17.5}Ti_{5.5}Al_{12.5}Co_{7.5}Ni_{12}Cu_{10}$ alloy. (c) XRD pattern and (d) EDX maps of Zr, Hf, Ti, Al, Co, Ni, and Cu in a $Zr_{35}Hf_{17.5}Ti_{5.5}Al_{12.5}Co_{7.5}Ni_{12}Cu_{10}$ alloy cast rod with a diameter of 18 mm prepared by tilt casting. The inset in (c) shows a photograph of the cast rod with a diameter of 18 mm.

Table 1
Maximum glass formation diameter (D_{max}) by casting, glass transition temperature (T_g) at 20 K/min, liquidus temperature (T_l) at 10 K/min, reduced glass transition temperature (T_g/T_l) and configuration entropy normalized by gas constant ($S_{config.}/R$) for the HE-BMGs developed by the present work. The data for previously reported Zr-based HE-BMG and BMGs with the formula of (ETM)-Al-(LTM) are shown for comparison.

	D_{max} (mm)	T_g (K)	T_l (K)	T_g/T_l	$S_{config.}/R$	Reference
$Zr_{56}Al_{16}Co_{28}$	18	741	1198	0.62	0.97	[23]
$Zr_{30}Hf_{25}Al_{20}Co_{25}$	5	802	1333	0.60	1.38	this work
$Zr_{30}Hf_{25}Al_{20}Co_{10}Ni_{10}Cu_5$	12	775	1337	0.58	1.64	this work
$Zr_{35}Hf_{17.5}Ti_{5.5}Al_{12.5}Co_{7.5}Ni_{12}Cu_{10}$	18	725	1206	0.60	1.77	this work
$Zr_{40}Hf_{10}Ti_4Y_1Al_{10}Cu_{25}Ni_7Co_2Fe_1$	14	679	–	–	1.66	[19]
$Zr_{57}Ti_5Al_{10}Cu_{20}Ni_8$	20	–	–	–	1.22	[32]
$Zr_{61}Ti_2Nb_2Al_{7.5}Ni_{10}Cu_{17.5}$	20	649	1157	0.56	1.19	[33]

lattice constants are slightly smaller. However, the compositions of the crystallized phases in the two alloys are quite different. The SEM-EDX composition analyses of the slowly solidified samples revealed that the Zr-BMG alloy is composed of $Zr_{51.1}Al_{7.9}Co_{41.0}$ (ZrCo phase) and $Zr_{65.4}Al_{23.1}Co_{11.5}$ (Zr_6Al_2Co phase), whereas the Zr-HE-BMG alloy is composed of $(Zr_{23.6}Hf_{24.0}Ti_{2.1})Al_{1.9}(Co_{16.0}Ni_{17.7}Cu_{14.7})$ (ZrCo phase) and $(Zr_{45.6}Hf_{18.6}Ti_{3.5})Al_{19.4}(Co_{5.5}Ni_{6.5}Cu_{0.9})$ (Zr_6Al_2Co phase). This indicates that Zr-HE-BMG crystallized into the ZrCo and Zr_6Al_2Co phases with more compositional complexity. Based on the above experimental results, the GFA of Zr–HE–BMG is now considered from the viewpoint of thermodynamics. The driving force for crystallization can be approximated by the difference of Gibbs free energy (ΔG) between the liquid phase and competing crystalline phases at a certain degree of undercooling [21,34]. For easier glass formation, smaller ΔG and thus a smaller driving force for crystallization is preferred. A similar analysis of the MD results was performed as for that of H. Fig. 4(b) shows calculated $\mathcal{H}$ for the amorphous, ZrCo, and Zr_6Al_2Co phases at 973 K for Zr–BMG and Zr–HE–BMG as a function of Co content. These calculations revealed that the difference in crystallization, $\Delta\mathcal{H}$, denoted by segment AE for Zr-HE-BMG was almost the same magnitude as that of Zr–BMG (~10 kJ/mol). This probably explains why Zr–HE–BMG had the same GFA as that of Zr–BMG despite its large difference in $S_{config.}$. However, because BMGs often crystallize through the formation of metastable phases, it is important to take this behavior into account in the thermodynamic evaluation. Additionally, because glass formation is affected by kinetics, it is important to consider kinetic processes such as diffusion to precisely understand the effect of high entropy on GFA. The results of kinetic investigations summarized in Table 2 illustrate that D_X values of Zr, Al, and Co decreased with multicomponent alloying in Zr–HE–BMG compared with those of the ternary Zr–BMG. It should be noted that D_{Al} of Zr–HE–BMG was only about half that of Zr–BMG. Furthermore, every value of D_X for the Zr-family elements—Zr, Hf, and even Ti, which has lighter atomic weight than that of Zr—exhibited smaller D_X values in Zr–HE–BMG than D_{Zr} in the ternary BMG. Similar tendencies were also seen in Zr–HE–BMG for D_{Ni} and D_{Cu} as well as D_{Co} for Co-family elements in Zr–HE–BMG; that is, D_{Co} was smaller in Zr–HE–BMG than in the ternary BMG. Table 2 indicates that multicomponent alloying induced by the high-entropy effect caused the decrease in D_X, suggesting sluggish crystallization and increased GFA. The above kinetic analysis based on D_X suggests that Zr–HE–BMG, which thermodynamically exhibited lower T_g/T_l than the prototypical ternary BMG, possessed the same GFA of $D_{max} = 18$ mm.

In conclusion, a new $Zr_{35}Hf_{17.5}Ti_{5.5}Al_{12.5}Co_{7.5}Ni_{12}Cu_{10}$ HE-BMG with a GFA reaching 18 mm and high S_{config} of $1.77R$ was efficiently developed by searching for a eutectic composition in the septenary alloy. This HE-BMG is different from the previously reported ones in that

Table 2
Self-diffusion coefficient of X element (D_X) for amorphous phase subjected to annealing at 973 K for 1 ps from values of mean square displacements of X element ($L_{MSD,X}$) with t [29].

	D_{Zr} (cm^2/s)	D_{Hf} (cm^2/s)	D_{Ti} (cm^2/s)	D_{Al} (cm^2/s)	D_{Co} (cm^2/s)	D_{Ni} (cm^2/s)	D_{Ni} (cm^2/s)
$Zr_{35}Hf_{17.5}Ti_{5.5}Al_{12.5}Co_{7.5}Ni_{12}Cu_{10}$	0.399508	0.444124	0.412767	0.399198	0.367341	0.489383	0.460646
$Zr_{56}Al_{16}Co_{28}$	0.470044	—	—	0.681942	0.5029066	—	—

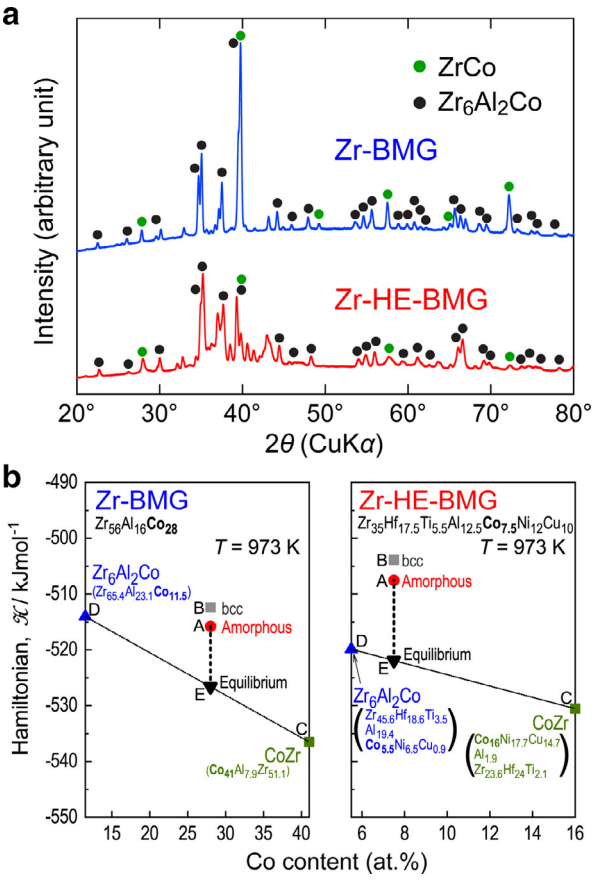

Fig. 4. (a) XRD patterns of (top) $Zr_{56}Al_{16}Co_{28}$ (Zr-BMG) and (bottom) $Zr_{35}Hf_{17.5}Ti_{5.5}Al_{12.5}Co_{7.5}Ni_{12}Cu_{10}$ (Zr-HE-BMG) alloy ribbons annealed for 12 h at 973 K, which is about 200 K higher than the crystallization temperature. (b) Calculated Hamiltonian ($\mathcal{H}$) for the amorphous, bcc, ZrCo and Zr_6Al_2Co phases for the Zr-BMG and Zr-HE-BMG at 973 K, as a function of Co content along the cross-sectional line connecting Zr_6Al_2Co and ZrCo compositions experimentally obtained by EDX composition analyses. The segment AE corresponds to decrease in H when crystallization takes place from the amorphous phase.

it has a non-equiatomic composition and is free from Be. The analysis of the alloys and phases revealed that the HE-BMG had almost the same difference in Hamiltonian between amorphous and competing crystalline phases as the reference ternary BMG, suggesting a lower driving force for crystallization. Indeed, the HE-BMG exhibited an excellent GFA of 18 mm in diameter, which is presumably caused by the sluggish diffusion even though it has lower T_g/T_l compared to that of the prototypical BMG.

Acknowledgements

This work was supported by a Grant-in-Aid for Scientific Research on Innovative Areas on High Entropy Alloys (grant number 18H05452) from the ministry of education, culture, sports, science and technology (MEXT), Japan and a Grant-in-Aid for Scientific Research (B) (grant number 17H03375) from Japan society for the promotion of science (JSPS).

Declaration of interest

None

References

[1] J.W. Yeh, S.K. Chen, S.J. Lin, J.Y. Gan, T.S. Chin, T.T. Shun, C.H. Tsau, S.Y. Chang, Nanostructured High-Entropy Alloys with Multiple Principal Elements: Novel Alloy Design Concepts and Outcomes, Adv. Eng. Mater. 6 (2004) 299.
[2] J.W. Yeh, Recent progress in high-entropy alloys, Ann. Chim. Sci. Mat. 31 (2006) 633.
[3] J.W. Yeh, Alloy Design Strategies and Future Trends in High-Entropy Alloys, JOM 65 (2013) 1759.
[4] Y. Zhang, T.T. Zuo, Z. Tang, M.C. Gao, K.A. Dahmen, P.K. Liaw, Z.P. Lu, Microstructures and properties of high-entropy alloys, Prog. Mater. Sci. 61 (2014) 1.
[5] M.C. Gao, J.-W. Yeh, P.K. Liaw, Y. Zhang (Eds.), High-Entropy Alloys, Fundamentals and Applications, Springer, Switzerland, 2016.
[6] A. Inoue, Stabilization of metallic supercooled liquid and bulk amorphous alloys, Acta Mater. 48 (2000) 279.
[7] W.L. Johnson, Bulk Glass-Forming Metallic Alloys: Science and Technology, MRS Bull. 24 (1999) 42.
[8] C. Suryanarayana, A. Inoue, Bulk Metallic Glasses, CRC press, 2010.
[9] L.Q. Ma, L.M. Wang, T. Zhang, A. Inoue, Bulk Glass Formation of Ti–Zr–Hf–Cu–M (M=Fe, Co, Ni) Alloys, Mater. Trans. 43 (2002) 277.
[10] A. Takeuchi, N. Chen, T. Wada, Y. Yokoyama, H. Kato, A. Inoue, J.W. Yeh, $Pd_{20}Pt_{20}Cu_{20}Ni_{20}P_{20}$ high-entropy alloy as a bulk metallic glass in the centimeter, Intermetallics 19 (2011) 1546.
[11] X.Q. Gao, K. Zhao, H.B. Ke, D.W. Ding, W.H. Wang, H.Y. Bai, High mixing entropy bulk metallic glasses, J. Non-Cryst. Solids 357 (2011) 3557.
[12] H.Y. Ding, K.F. Yao, High entropy $Ti_{20}Zr_{20}Cu_{20}Ni_{20}Be_{20}$ bulk metallic glass, J. Non-Cryst. Solids 364 (2013) 9.
[13] S.F. Zhao, Y. Shao, X. Liu, N. Chen, H.Y. Ding, K.F. Yao, Pseudo-quinary $Ti_{20}Zr_{20}Hf_{20}Be_{20}(Cu_{20-x}Ni_x)$ high entropy bulk metallic glasses with large glass forming ability, Mater. Des. 87 (2015) 625.
[14] S.F. Zhao, G.N. Yang, H.Y. Ding, K.F. Yao, A quinary Ti–Zr–Hf–Be–Cu high entropy bulk metallic glass with a critical size of 12 mm, Intermetallics 61 (2015) 47.
[15] H.Y. Ding, Y. Shao, P. Gong, J.F. Li, K.F. Yao, A senary TiZrHfCuNiBe high entropy bulk metallic glass with large glass-forming ability, Mater. Lett. 125 (2014) 151.
[16] L.S. Huo, H. Men, X.M. Wang, A. Inoue, J.Q. Wang, C.T. Chang, R.W. Li, The magnetocaloric effect of Gd-Tb-Dy-Al-M (M = Fe, Co and Ni) high-entropy bulk metallic glasses, Intermetallics 58 (2015) 31.
[17] T. Qi, Y. Li, A. Takeuchi, G. Xie, H. Miao, W. Zhang, Soft magnetic $Fe_{25}Co_{25}Ni_{25}(B, Si)_{25}$ high entropy bulk metallic glasses, Intermetallics 66 (2015) 8.
[18] Y. Xu, Y. Li, Z. Zhu, W. Zhang, Formation and properties of $Fe_{25}Co_{25}Ni_{25}(P, C, B, Si)_{25}$ high-entropy bulk metallic glasses, J. Non-Cryst. Solids 487 (2018) 60.
[19] C. Chen, S. Pang, Y. Cheng, T. Zhang, A centimeter-size $Zr_{40}Hf_{10}Ti_4Y_1Al_{10}Cu_{25}Ni_7Co_2Fe_1$ bulk metallic glass with high mixing entropy designed by multi-substitution, J. Non-Cryst. Solids 410 (2015) 39.
[20] A.L. Greer, Confusion by design, Nature 366 (1993) 303.
[21] R. Busch, J. Schroers, W.H. Wang, Thermodynamics and Kinetics of Bulk Metallic Glass, MRS Bull. 32 (2007) 620.
[22] Y. Yokoyama, H. Inoue, K. Fukaura, A. Inoue, Relationship Between the Liquidus Surface and Structures of Zr-Cu-Al Bulk Amorphous Alloys, Mater. Trans. 43 (2002) 575.
[23] T. Wada, F.X. Qin, X.M. Wang, M. Yoshimura, A. Inoue, N. Sugiyama, R. Ito, N. Matsushita, Formation and bioactivation of Zr-Al-Co bulk metallic glasses, J. Mater. Res. 24 (2011) 2941.
[24] D.B. Miracle, A structural model for metallic glasses, Nature Mater. 3 (2004) 697.
[25] J. Kim, H.S. Oh, J. Kim, C.W. Ryu, G.W. Lee, H.J. Chang, E.S. Park, Utilization of high entropy alloy characteristics in Er-Gd-Y-Al-Co high entropy bulk metallic glass, Acta Mater. 155 (2018) 350.
[26] FUJITSU Technical Computing Solution SCIGRESS, https://www.fujitsu.com/global/solutions/business-technology/tc/sol/scigress/, 2019 (accessed 10 June 2019). http://www.fujitsu.com/global/solutions/business-technology/tc/sol/scigress/
[27] K.H.J. Buschow, Crystallization of amorphous $Zr_{1-x}Co_x$ alloys, J. Less-Common Met. 85 (1982) 221.
[28] M.S. Daw, M.I. Baskes, Embedded-atom method: Derivation and application to impurities, surfaces, and other defects in metals, Phys. Rev. B 29 (1984) 6443.

[29] A. Takeuchi, K. Yubuta, T. Wada, Critically Percolated States in High-Entropy Alloys with Exact Equi-Atomicity, Mater. Trans. 60 (2019) 330.
[30] C. Colinet, J.-C. Crivello, J.-C. Tedenac, Structural stability of ternary C22–Zr_6X_2Co (X=Al, Ga, Sn, As, Sb, Bi, Te) and C22–Zr_6Sn_2T' (T'=Fe, Co, Ni, Cu) compounds, J. Solid State Chem. 205 (2013) 217.
[31] A. Makino, P. Sharma, K. Sato, A. Takeuchi, Y. Zhang, K. Takenaka, Artificially produced rare-earth free cosmic magnet, Sci. Rep. 5 (2015) 16627.
[32] L.Q. Xing, P. Ochin, Bulk glass formation in the Zr-Ti-Al-Cu-Ni system, J. Mater. Sci. Lett. 16 (1997) 1277.
[33] A. Inoue, Q.S. Zhang, W. Zhang, K. Yubuta, K.S. Son, X.M. Wang, Formation, Thermal Stability and Mechanical Properties of Bulk Glassy Alloys with a Diameter of 20 mm in Zr-(Ti,Nb)-Al-Ni-Cu System, Mater. Trans. 50 (2009) 388.
[34] X.L. Ji, Y. Pan, Gibbs free energy difference in metallic glass forming liquids, J. Non-Cryst. Solids 353 (2007) 2443.